Chemical Science

ROYAL SOCIETY OF CHEMISTRY

EDGE ARTICLE

View Article Online
View Journal | View Issue

Cite this: *Chem. Sci.*, 2020, **11**, 4397

All publication charges for this article have been paid for by the Royal Society of Chemistry

Received 12th February 2020
Accepted 30th March 2020

DOI: 10.1039/d0sc00844c

rsc.li/chemical-science

A pH ratiometrically responsive surface enhanced resonance Raman scattering probe for tumor acidic margin delineation and image-guided surgery†

Wenjia Duan,‡[a] Qi Yue,‡[b] Ying Liu,‡[c] Yunfei Zhang,[a] Qinghua Guo,[a] Cong Wang,[a] Shujie Yin,[a] Dandan Fan,[a] Wenjing Xu,[c] Jiexian Zhuang,[a] Jiachao Gong,[d] Xinwei Li,[a] Ruimin Huang,[e] Liang Chen,[b] Silvio Aime,[f] Zhongliang Wang,[g] Jianfeng Feng,[c] Ying Mao,*[b] Xiao-Yong Zhang*[c] and Cong Li*[a]

Surgery remains the mainstay for most solid tumor treatments. However, surgeons face challenges in intra-operatively identifying invasive tumor margins due to their infiltrative nature. Incomplete excision usually leads to early recurrence, while aggressive resection may injure adjacent functional tissues. Herein, we report a pH responsive ratiometric surface-enhanced Raman scattering (SERRS) probe that determined physiological pHs with a high sensitivity and tissue penetration depth *via* an innovative mechanism named spatial orientation induced intramolecular energy transfer (SOIET). Due to the positive correlation between tumor acidity and malignancy, an acidic margin-guided surgery strategy was implemented in live animal models by intra-operatively assessing tissue pH/malignancy of the suspicious tissues in tumor cutting edges. This surgery remarkably extended the survival of animal models and minimized their post-surgical complications, showing promise in precisely identifying invasive tumor boundaries and achieving a balance between maximum tumor debulking and minimal functional impairment.

Introduction

Surgery is a mainstream treatment for solid tumors. The goal for infiltrative tumor surgery is the maximal resection of the tumor tissue because the extent of resection is positively proportional to patient survival.[1] However, the infiltrative regions developed by the invasion of cancer cells along the micronerves and capillaries are difficult to identify intraoperatively. Therefore, the precise delineation of tumor infiltrative territories remains a pivotal concern in improving surgical prognosis.

Clinically used techniques such as neuro-navigation and intra-operative magnetic resonance imaging (iMRI) rely on paramagnetic gadolinium chelators for delineating the tumor margin. However, this margin actually presents the territory with disrupted vasculatures instead of the actual infiltrative region leading to tumor recurrence. Tumor associated metabolites present the proliferative, invasive and metastatic natures of cancer cells. The intratumoral choline (Cho) to *N*-acetyl aspartate (NAA) ratio determined by magnetic resonance spectroscopy (MRS) had been used in clinics to evaluate malignancies of primary central nervous system lymphoma and the brain tumor.[2] However, the translation of Cho/NAA ratio guided surgery is hindered by the low spatial resolution and extended acquisition time of MRS.[3] Nevertheless, intra-operative imaging of tumor associated metabolites shows promise in guiding tumor resection. The metabolic switch from oxidative phosphorylation to aerobic glycolysis (Warburg effect) in cancer cells results in the acidification of the tumor extracellular microenvironment (pH 6.2–6.9).[4] Gillies *et al.* found that the peritumoral regions with the highest invasiveness corresponded to the areas with the lowest extracellular pH (pH_e).[5] Gertler *et al.* showed that acidification in tumor boundaries drove transcriptome dynamics to promote the acquisition of invasive phenotypes.[6] Therefore, intra-operative determination of acidities in tumor

[a]*Key Laboratory of Smart Drug Delivery, Ministry of Education, School of Pharmacy, Fudan University, Shanghai 201203, China. E-mail: congli@fudan.edu.cn*

[b]*Department of Neurosurgery, Huashan Hospital, Fudan University, Shanghai 200040, China. E-mail: maoying@fudan.edu.cn*

[c]*Key Laboratory of Computational Neuroscience and Brain-Inspired Intelligence, Ministry of Education, Institute of Science and Technology for Brain-Inspired Intelligence, Fudan University, Shanghai 200433, China. E-mail: xiaoyong_zhang@fudan.edu.cn*

[d]*Bejing Laboratory of Intelligent Information Technology, School of Computer Science and Technology, Beijing Institute of Technology, Beijing 100081, China*

[e]*Shanghai Institute of Materia Medica, Chinese Academy of Sciences, Shanghai 201203, China*

[f]*Department of Molecular Biotechnologies, Health Sciences Molecular Imaging Center, University of Torino, Via Nizza 52, 10126 Torino, Italy*

[g]*Engineering Research Center of Molecular & Neuroimaging, Ministry of Education, School of Life Science and Technology, Xidian University, Xi'an, Shaanxi 710026, China*

† Electronic supplementary information (ESI) available. See DOI: 10.1039/d0sc00844c

‡ These authors contributed equally to this work.

cutting edges holds promise in locating and excising the infiltrative region with high malignancy.

Raman imaging is an optical spectroscopic technology that describes the chemical composition of samples by monitoring the inelastic scattering generated from the interaction between the incident light and virtual energy states of the sample.[7] The Raman signal could be massively enhanced by 10^8 to 10^{12} fold *via* a surface-enhanced Raman scattering (SERS) effect.[8] Compared with fluorescence imaging, SERS shows higher photo-stability, higher sensitivity and multiplexing potential for the detection of up to ten targeting compounds simultaneously.[9,10] Multi-modality or ultra-sensitive SERS probes have been reported to outline tumor infiltrative margins and microscopic malignant foci.[11,12] However, these probes visualizing tumor margins *via* the enhanced permeability and retention (EPR) effect cannot fully delineate tumor invasive regions with high acidity.[13] A few pH-responsive SERS probes were reported to define tumors by sensing their acidic environments,[14] but their intensity-dependent readout is easily interrupted by uneven probe concentrations induced by tumor heterogenicity, resulting in erroneous detection readouts. There has been growing interest in ratiometric probes that acquire quantitative information for the analyte *via* built-in self-calibration.[15] By this method, the artifical errors caused by heterogeneous probe difussion and distribution could be minimized. Therefore, the pH ratiometrically responsive SERS probe holds promise in locating tumor infiltrative regions by quantitatively determining the pHs/malignancies in tumor cutting edges.

In this work, a novel ratiometric SERRS design strategy was reported and a pH ratiometrically responsive SERRS probe **AuS-IR7p** was developed, which independently determined pH values with high sensitivity, accuracy and reversibility. With assistance of this probe, an acidic margin-guided tumor resection surgery strategy was proposed by intra-operatively assessing tissue malignancies in live animal models *via* real-time determination of pH values (Fig. 1A). Furthermore, surgical prognosis was dynamically evaluated by non-invasive contrast enhanced MRI (CE-MRI). The acidic margin-guided surgery strategy using **AuS-IR7p** shows promise in identifying invasive glioma boundaries and achieving a balance between maximum tumor debulking and minimal functional impairment.

Results and discussion

Synthesis and characterization of AuS-IR7p

Gold nanostars were chosen as the substrate for the SERS probe due to the followingreasons. First, numerous sharp tips on the probe surface can trigger 2–3 orders of magnitude extra signal enhancement due to the hotspot effect.[16] Second, the overlapping between the plasmon absorption of gold nanostars (700–800 nm) and the energy of the incident laser (785 nm) remarkably increases the signal intensity.[17] Heptamethine cyanine derivative **IR7** was chosen as a Raman molecular reporter because its absorption maxima (760–790 nm) matches with that of the incident laser (785 nm), which triggers the surface enhanced resonance Raman scattering (SERRS) effect[18] and leads to extra 1–3 orders of magnitude signal enhancement

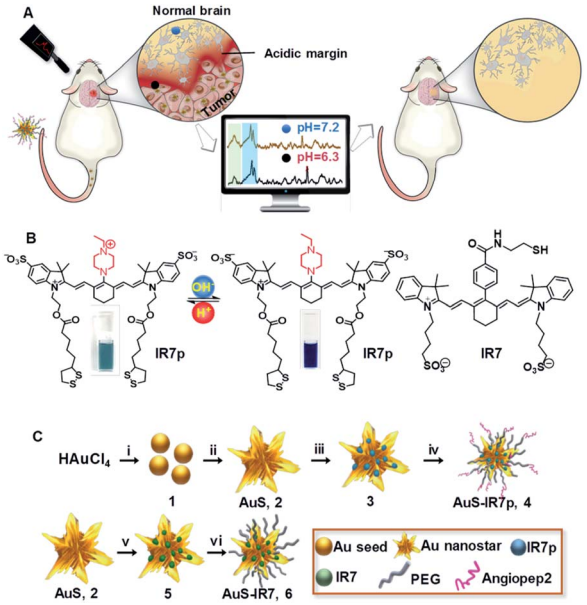

Fig. 1 Design and synthesis of the pH ratiometrically responsive SERRS probe. (A) Illustration presenting the acidic margin-guided brain tumor surgery by intra-operatively determining tissue pH values/malignancies in tumor cutting edges. (B) Chemical structure of the pH-responsive reporter molecule **IR7p** and the control reporter **IR7** without pH sensitivity. (C) Synthesis of pH responsive SERRS probe **AuS-IR7p** and the control probe **AuS-IR7**. (i) Sodium citrate; (ii) ascorbic acid, $AgNO_3$; (iii) **IR7p**; (iv) HS-PEG^{5K}-NHS, cysteine-modified angiopep2 peptide; (v) **IR7**; (vi) HS-PEG^{5K}-OMe.

compared to non-resonance SERS. Additionally, the probe surface was modified with angiopep2 peptides to facilitate its brain delivery by traversing the BBB *via* low-density lipoprotein-receptor-related protein-1 (LRP1) mediated receptor-mediated endocytosis (RMT).[19]

The synthesis of the pH ratiometrically responsive SERRS probe **AuS-IR7p** is presented in Fig. 1B and C. Briefly, the reaction between citrate and chloroauric acid yielded spherical gold seeds **1** with an average diameter of 12 nm. The asymmetric growth of the gold seeds in a mixture of chloroauric acid, ascorbic acid and $AgNO_3$ offered gold nanostars AuS (**2**) possessing multiple outward gold spikes.[20] The surface modification of AuS with **IR7p** through the Au–S covalent bonds gave nanoparticles **3**. Similarly, fabrication of HS-PEG^{5K}-OMe and angiopep2-PEG-SH on **3** with a molar ratio of 10 : 1 offered the final product **AuS-IR7p** (**4**). Meanwhile, control SERRS probe **AuS-IR7** (**6**) was prepared by surface modification of AuS with molecule reporter **IR7** that has a similar chemical structure to **IR7p** but without the pH sensitivity. Transmission electron microscopy (TEM) images showed **AuS-IR7p** dispersed with an average diameter of 50 nm (Fig. 2A). Dynamic light scattering (DLS) determined the average hydrodynamic particle size of **AuS-IR7p** to be 132.0 nm and its zeta potential to be 8.2 mV (Fig. 2B). *In vitro* confocal Raman imaging studies demonstrated the acidity triggered SERRS signal enhancement of **AuS-IR7p** and an extremely low detection limit of 0.8 pM was observed at pH 5.5 (Fig. 2C and D). Notably, **AuS-IR7p** showed

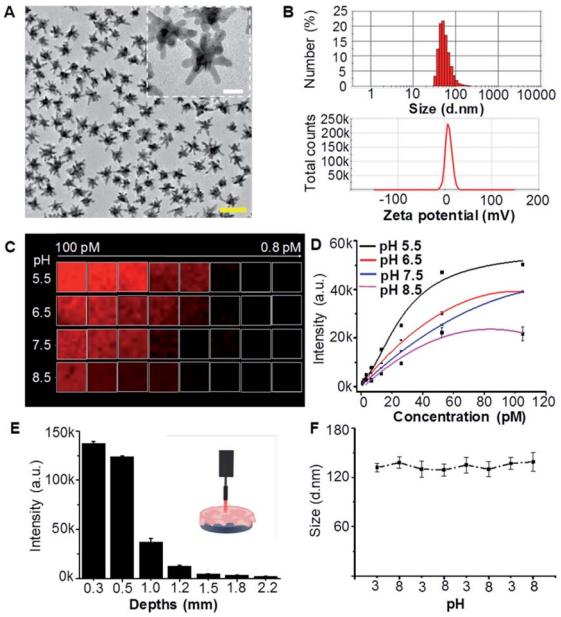

Fig. 2 Characterization of **AuS-IR7p**. (A) TEM image of **AuS-IR7p**. Scale bar = 100 nm. Inset: amplified gold nanostars. Scale bar = 20 nm. (B) Hydrodynamic diameter distribution and zeta potentials of **AuS-IR7p** in PBS solution (pH 7.4). (C) Raman microscopy image of **AuS-IR7p** as functions of concentrations and pH values by quantifying its characteristic peak at 510 cm^{-1}. (D) Concentration dependent Raman signal intensities of **AuS-IR7p** in buffered solutions with different pH values. (E) Raman signal intensities of **AuS-IR7p** as a function of the thickness of covered mouse brain tissue (200 mW laser power density, 1.0 s acquirement time, and 10× objective). Data are presented as mean ± S.D. (n = 3). (F) **AuS-IR7p** shows reversible pH responsive ability. The initial concentration was 100 pM. Laser power: 80 mW. Acquirement time: 1.0 s.

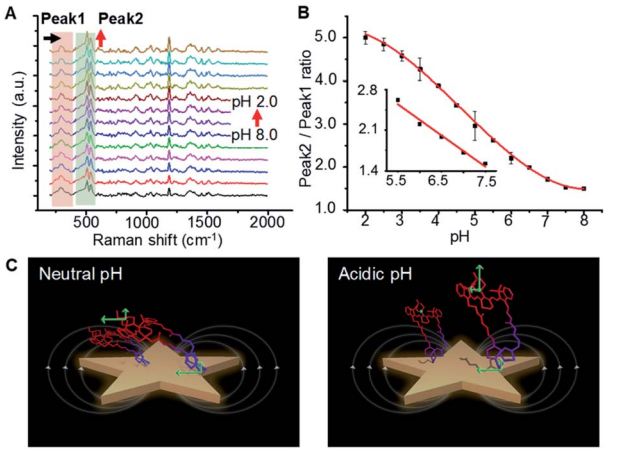

Fig. 3 **AuS-IR7p** determines pH values *via* ratiometrically responsive Raman signals. (A) pH dependent Raman spectra of **AuS-IR7p**. The pH changed with an interval of 0.5 units. (B) Plot of integrated intensity ratios between Raman Peak 2 (450–595 cm^{-1}) and Peak 1 (280–370 cm^{-1}) as a function of pH. The inset shows measurements in the linear response region. (C) Proposed mechanism illustrating the pH ratiometric response of **AuS-IR7p**. Unprotonated **IR7p** shows parallel conformation relative to the metallic surface (left panel) but titled or even perpendicular conformation under acidic conditions (right panel) due to the intermolecular electrostatic repulsion triggered by the protonation of reporter molecule **IR7p**.

a high tissue penetration depth and its Raman signal was detected even when covered by mouse brain tissue with a thickness of 2.2 mm (Fig. 2E). **AuS-IR7p** could reversibly monitor the pH variation in the physiological range even after four switching cycles from pH 3 to pH 8 (Fig. S1†). Besides, the average hydrodynamic particle size remained around 130 nm after four pH switching cycles, which verifies the minimized self-aggregation of this SERRS probe (Fig. 2F). **AuS-IR7p** showed minimized cytotoxicity after culturing with microglial, neuronal and endothelial cell lines (Fig. S2 and S3†).

pH ratiometric responses of AuS-IR7p

Raman reporter molecule **IR7p** demonstrated pH-responsive absorbance in the near-infrared (NIR) wavelength range (Fig. S4†). Obvious bathochromic shift with a new peak centered at 770 nm was monitored when the pH decreased to 2.0 from 8.0. Protonation of nitrogen in the ethylpiperazidine group results in a decreased intramolecular energy gap and thus produces the bathochromic shift ofabsorption. As expected, the absorbance of **IR7** remained unchanged from pH 8.0 to pH 3.0 (Fig. S5†). Fig. 3A shows the Raman spectra of **AuS-IR7p** as a function of pH after excitation at 785 nm. The peak at 311 cm^{-1} could be assigned to the Au–S stretching and bending. The sharp twin peaks at 527 and 558 cm^{-1} could be attributed to the ring deformation of the methylene carbon chain. The bands at 784 and 927 cm^{-1} represent C–H out-of-plane bending mode and C–C symmetric stretching mode of the methylene carbon chain. A peak at 1511 cm^{-1} could be assigned to the C=O stretching in ester bonds, and a peak at 1199 cm^{-1} could be assigned to the C–N stretching in the ethylpiperazine ring. Interestingly, while most of the Raman signatures increased gradually upon acidification, the peak at 311 cm^{-1} (highlighted as Peak 1) remained steady. Notably, the Raman intensity ratio between the twin peak (highlighted as Peak 2) and Peak 1 increased from 1.5 to 5.0 when the pH decreased from 8.0 to 2.0. Plotting the Peak 2/Peak 1 ratio against the pH value offered a pK_a value of 4.6 for **AuS-IR7p** (Fig. 3B). Confocal Raman spectroscopic images of **AuS-IR7p** showed that while the integrated intensity of Peak 2 increased with acidification, the intensity of Peak 1 remained stable (Fig. S6†). Significantly, the pH values determined by **AuS-IR7p** (100 pM) coincide well with the value measured using a pH meter, especially in the range of pH 5.0–8.0 (Fig. S7†).

Three ratiometric SERS strategies had been reported to quantitatively determine the analyte concentration *in vivo*. The first is simultaneous injection of two probes in which one acts as a control to offset the nonspecific accumulation and the other is applied for analyte sensing.[21] The second is the incorporation of two or more types of Raman reporters into a particle, in which one inert reporter serves as an internal reference and the others are used for analyte determination.[22] The third is conjugation of a single reporter molecule being functionalized as both an analyte sensor and a self-built-in calibrator. As far as we are aware, **AuS-IR7p** is the first Raman probe independently determining

physiological pH values with a signal reporter molecule. By this method, the measurement errors induced by the diverse pharmacokinetics of the different probes in the first and second strategies could be minimized. The mechanism of ratiometric responsiveness of **AuS-IR7p** was defined as a spatial orientation induced intramolecular energy transfer (SOIET) (Fig. 3C). The SERRS efficiency is highly dependent on the distance between the reporter molecule and metallic surface ($I_{SERRS} \sim r^{-12}$). Protonation of the reporter molecule **IR7p** increases the intermolecular electrostatic repulsion and triggers their orientations from flat to tilted or even perpendicular attitudes relative to the metallic surface. Vibration bonds in the reporter molecule backbone experienced a much more increased perpendicular polarizability tensor upon the electromagnetic field than Au–S bonds that directly conjugated on the metallic surface.

Acidic margin guided brain tumor resection in live rat models with AuS-IR7p

Acidic margin-guided surgery was conducted in live rat models bearing orthotopic C6 glioblastoma allografts with high invasiveness. *In vivo* T2W MR images showed the tumor with an average volume of 60–95 mm^3 (Fig. 4A). The *In vivo* pH map generated by chemical exchange saturation transfer (CEST)-MRI demonstrated the pronounced acidosis in the tumor but barely in the normal brain (Fig. 4B). The average pH value of 6.6 was measured in the tumor in comparison to 7.2 in the normal brain. Craniotomy was conducted in the right frontoparietal region (Fig. 4C). Animal models were randomly divided into three groups: (1) intra-operative acidic margin (iAM) guided surgery after intravenous (i.v.) injection of **AuS-IR7p**, (2) intra-operative structural margin (iSM) guided surgery after i.v. injection of **AuS-IR7** and (3) preoperative structural margin (pSM) guided surgery after i.v. injection of Gd^{3+}-DTPA. A handheld Raman spectrometer was used to intra-operatively collect the Raman signal due to its capability to scan the operation bed with high flexibility and velocity. Additionally, with assistance of home-made software that automatically identifies the characteristic Raman peaks and converts the Peak 2/Peak 1 ratio into a pH value, the acidity of a suspicious tissue spot can be obtained in 5 s. In the iAM-guided surgery group, the acidosis distribution pattern at tumor cutting edges was presented as a 3D pixel block map, in which each pixel block presented the pH value of the measured point (1 × 1 × 1 mm). Guided by the pH map, the acidic tissues were excised step by step until no foci with pH below 7.0 could be detected (Fig. 4D). In the iSM-guided group, the tissues detected with characteristic Raman signals of **AuS-IR7** were excised continuously until no signal in the operation bed was identified. In the pSM-guided group, the tumor was resected according to the margin delineated by the pre-operative MRI.

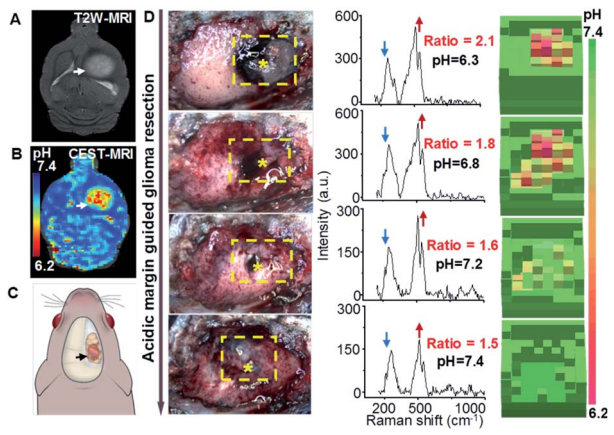

Fig. 4 Acidic margin-guided brain tumor surgery in live rat models. (A) Preoperative T2W-MR image of rat brain bearing C6 orthotopic allografts. The tumor was indicated by a white arrow. (B) *In vivo* CEST-pH map of a rat brain model. (C) Illustration indicating the surgical location before the craniotomy. (D) Sequential white light images (left panel), intra-operatively collected Raman spectra (middle panel) and a pH topographic map (right panel) of the resection bed. Yellow dashed boxes marked the area with detectable SERRS signals and star symbols presented the points with the highest acidity.

Acidic margin guided surgery improving surgical prognosis

Fig. 5A presents *in vivo* MR images of mouse brains before and on selected days post the above intervention. In the pSM-guided

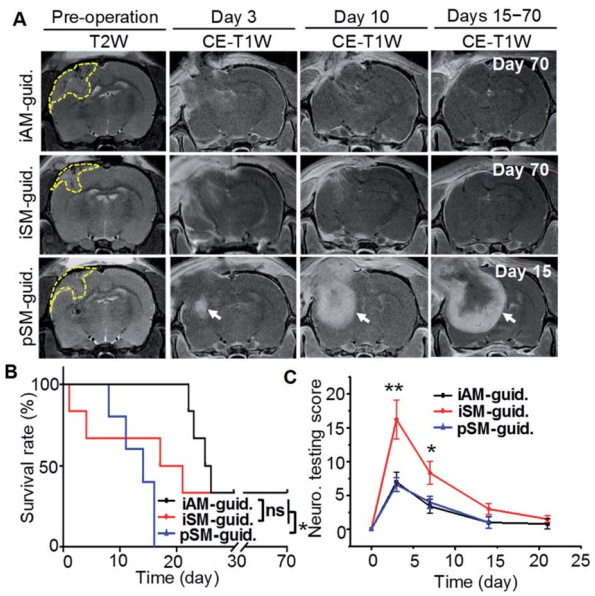

Fig. 5 Intra-operative acidic margin-guided surgery improves surgical prognosis and minimizes functional deficits. (A) *In vivo* MR images of a rat brain bearing C6 rat orthotopic allografts before and at selected days post iAM-guided, iSM-guided and pSM-guided surgery. Tumors with hyper-intensive signals in the preoperative T2W-MR images were delineated by yellow dotted lines. The recurrent tumor was indicated by a white arrow. Kaplan–Meier survival (B) and neurological testing scores (C) after corresponding surgical intervention. Data were presented as mean ± S.D. ($n = 5$). $^{**}p < 0.01$ between the iAM-, iSM-guided strategy and pSM-guided surgery. ns, no significant difference. In panel E, $^{**}p < 0.01$ and $^{*}p < 0.05$ between the iAM- and iSM-guided groups on day 3 and 7. iAM-guid.: intra-operative acidic margin guided surgery; iSM-guid.: intra-operative structure margin guided surgery; pSM-guid.: preoperative structural margin guided surgery. CE-T1W: contrast enhanced T1-weighted.

group, rapid tumor relapse was observed as early as 3 days post-surgery and the recurrent neoplastic tissue was observed in all models on day 15. In contrast, obvious tumor recurrences were not detected on day 15 post iAM- or iSM-guided groups (Fig. S8A†). The Kaplan–Meier survival curve showed that all models in the pSM-guided group died before day 16 (Fig. 5B), which was explained by the incomplete tumor resection. For the iSM-guided group, one third of the models died within three days, which resulted from functional disabilities and another one-third died gradually with concomitant tumor recurrence. Remarkably, no animal death was monitored until 21 days post the iAM-guided surgery and one-third of the animals survived more than 90 days without tumor recurrence. The iAM-guided group also showed the highest post-operative recovery (Fig. S8B†). Neurological Assessment (NA) quantitatively determined the neurological functional deficits with respect to reflexes (normal score: 0, maximal deficit score: 21) (Fig. 5C). Although all three groups showed their maximal NA scores on day 3, the NA score of the iAM-guided group remained the lowest.

Conclusions

In conclusion, by developing a pH ratiometrically responsive SERRS probe, we first propose an acidic margin-guided surgery strategy, which remarkably extends the overall survival of animal models and minimizes postoperative complications. Considering the correlation between the acidity and malignancy in tumor tissues, this strategy will help surgeons to demarcate tumor infiltrated regions that are usually "invisible" in the clinically used surgical navigation systems and achieve a balance between maximum tumor debulking and minimal functional impairment. Additionally, this acidic margin-guided surgery strategy holds promise in the treatment of different types of infiltrated tumors because extracellular acidification is a hallmark of solid tumors regardless of their genotypes or phenotypes.

Ethical statement

All animal studies were performed in compliance with the guidelines set by the Chinese Committee of Management of Laboratory Animals and the overall project protocols were approved by the Ethics Committee of Fudan University.

Conflicts of interest

There are no conflicts to declare.

Acknowledgements

This work was supported by the National Natural Science Foundation of China (No. 81771895 to C. L.; 81572483 and 81611130223 to Y. M.; 81873893 to X. Z.; 81602178 to Q. Y.; 81671753 to Z. W.; 81771890 and 91859106 to R. H.), the Program of Shanghai Science and Technology Committee (No. 19431900400 and 18441900600 to C. L., 13411950201 and 16JC1420100 to Y. M.), the Fudan-SIMM Joint Research Fund (No. 20173001 to C. L. and R. H.), the One Hundred Talent Program of the Chinese Academy of Sciences (to R. H.), the Shanghai Municipal Science and Technology Major Project (No. 2018SHZDZX01 to J. F. and X. Z., 2018SHZDZX03 to Y. M.), the 111 Project (No. B18015 to J. F.) and the Zhangjiang Lab.

Notes and references

1 M. G. Matthew, F. R. Pablo, S. N. Amy, L. S. Jason, A. Lilyana, H. B. Gene and A. V. Michael, *J. Neurosurg.*, 2014, **121**, 1115–1123.
2 M. Bulik, R. Jancalek, J. Vanicek, A. Skoch and M. Mechl, *Clin. Neurol. Neurosurg.*, 2013, **115**, 146–153.
3 J. Zhang, D. X. Zhuang, C. J. Yao, C. P. Lin, T. L. Wang, Z. Y. Qin and J. S. Wu, *J. Neurosurg.*, 2016, **124**, 1585–1593.
4 R. J. Gillies, Z. Liu and Z. Bhujwalla, *Am. J. Physiol.*, 1994, 267.
5 V. Estrella, T. Chen, M. Lloyd, J. Wojtkowiak, H. H. Cornnell, A. Ibrahim-Hashim, K. Bailey, Y. Balagurunathan, J. M. Rothberg, B. F. Sloane, J. Johnson, R. A. Gatenby and R. J. Gillies, *Cancer Res.*, 2013, **73**, 1524.
6 N. Rohani, L. L. Hao, M. S. Alexis, B. A. Joughin, K. Krismer, M. N. Moufarrej, A. R. Soltis, D. A. Lauffenburger, M. B. Yaffe, C. B. Burge, S. N. Bhatia and F. B. Gertler, *Cancer Res.*, 2019, **79**, 1952–1966.
7 K. Kong, C. Kendall, N. Stone and I. Notingher, *Adv. Drug Delivery Rev.*, 2015, **89**, 121–134.
8 L. A. Lane, X. Qian and S. Nie, *Chem. Rev.*, 2015, **115**, 10489–10529.
9 C. L. Zavaleta, B. R. Smith, I. Walton, W. Doering, G. Davis, B. Shojaei, M. J. Natan and S. S. Gambhir, *Proc. Natl. Acad. Sci. U. S. A.*, 2009, **106**, 13511–13516.
10 Y. Qiu, Y. Zhang, M. Li, G. Chen, C. Fan, K. Cui, J.-B. Wan, A. Han, J. Ye and Z. Xiao, *ACS Nano*, 2018, **12**, 7974–7985.
11 M. F. Kircher, A. de la Zerda, J. V. Jokerst, C. L. Zavaleta, P. J. Kempen, E. Mittra, K. Pitter, R. Huang, C. Campos, F. Habte, R. Sinclair, C. W. Brennan, I. K. Mellinghoff, E. C. Holland and S. S. Gambhir, *Nat. Med.*, 2012, **18**, 829–834.
12 H. Karabeber, R. M. Huang, P. Iacono, J. M. Samii, K. Pitter, E. C. Holland and M. F. Kircher, *ACS Nano*, 2014, **8**, 9755–9766.
13 S. Harmsen, R. Huang, M. A. Wall, H. Karabeber, J. M. Samii, M. Spaliviero, J. R. White, S. Monette, R. O'Connor, K. L. Pitter, S. A. Sastra, M. Saborowski, E. C. Holland, S. Singer, K. P. Olive, S. W. Lowe, R. G. Blasberg and M. F. Kircher, *Sci. Transl. Med.*, 2015, **7**, 271ra277.
14 T. Zhao, G. Huang, Y. Li, S. Yang, S. Ramezani, Z. Lin, Y. Wang, X. Ma, Z. Zeng, M. Luo, E. de Boer, X. J. Xie, J. Thibodeaux, R. A. Brekken, X. Sun, B. D. Sumer and J. Gao, *Nat. Biomed. Eng.*, 2016, **1**, 0006.
15 X. L. Huang, J. B. Song, B. C. Yung, X. H. Huang, Y. H. Xiong and X. Y. Chen, *Chem. Soc. Rev.*, 2018, **47**, 2873–2920.
16 L. Rodríguez-Lorenzo, R. A. Álvarez-Puebla, I. Pastoriza-Santos, S. Mazzucco, O. Stéphan, M. Kociak, L. M. Liz-Marzán and F. J. García de Abajo, *J. Am. Chem. Soc.*, 2009, **131**, 4616–4618.

17 H. Yuan, A. M. Fales, C. G. Khoury, J. Liu and T. Vo-Dinh, *J. Raman Spectrosc.*, 2013, **44**, 234–239.
18 S. Schlücker, *Angew. Chem., Int. Ed.*, 2014, **53**, 4756–4795.
19 H. Yan, L. Wang, J. Wang, X. Weng, H. Lei, X. Wang, L. Jiang, J. Zhu, W. Lu, X. Wei and C. Li, *ACS Nano*, 2012, **6**, 410–420.
20 L. Han, W. Duan, X. Li, C. Wang, Z. Jin, Y. Zhai, C. Cao, L. Chen, W. Xu, Y. Liu, Y. Y. Bi, J. Feng, Y. Mao, Q. Yue, X. Y. Zhang and C. Li, *ACS Appl. Mater. Interfaces*, 2019, **11**, 15241–15250.
21 Y. W. Wang, N. P. Reder, S. Kang, A. K. Glaser, Q. Yang, M. A. Wall, S. H. Javid, S. M. Dintzis and J. T. C. Liu, *Cancer Res.*, 2017, **77**, 4506–4516.
22 S. Ye, X. Li, M. Wang and B. Tang, *Anal. Chem.*, 2017, **89**, 5124–5130.